

# Relics in medieval altarpieces? Combining X-ray tomographic, laminographic and phase-contrast imaging to visualize thin organic objects in paintings

Kris Krug,<sup>a</sup> Liisa Porra,<sup>b,c</sup> Paola Coan,<sup>b</sup> Arie Wallert,<sup>d</sup> Joris Dik,<sup>a\*</sup> Andrea Coerdts,<sup>d</sup> Alberto Bravin,<sup>b</sup> Muthaffar Elyyan,<sup>e</sup> Péter Reischig,<sup>a,b</sup> Lukas Helfen<sup>e,b</sup> and Tilo Baumbach<sup>e</sup>

<sup>a</sup>Department of Materials Science and Engineering, Delft University of Technology, Delft, The Netherlands, <sup>b</sup>European Synchrotron Radiation Facility, Grenoble, France, <sup>c</sup>Department of Physical Sciences, University of Helsinki, Finland, <sup>d</sup>Rijksmuseum, Amsterdam, The Netherlands, and <sup>e</sup>ANKA/ISS, Forschungszentrum Karlsruhe, Germany. E-mail: j.dik@tudelft.nl

X-ray radiography is a common tool in the study of old master paintings. Transmission imaging can visualize hidden paint layers as well as the structure of the panel or canvas. In some medieval altarpieces, relics seem to have been imbedded in the wooden carrier of paintings. These are most probably thin organic fibrous materials such as paper or textile, which in traditional radiography are shadowed by the more absorbing surrounding material. This paper studies the application potential of synchrotron-based tomographic and laminographic imaging complemented with phase-contrast imaging for detection of such relics. The techniques are applied to a dummy painting. The results demonstrate that by using these imaging methods it is possible to three-dimensionally visualize hidden cavities in panels and detect thin fibrous low-Z materials sandwiched between a high-Z paint layer and a thick wooden panel.

**Keywords:** paintings; X-ray; imaging; phase contrast; tomography; laminography.

## 1. Introduction

During the Middle Ages, Christianity attached great value to relics, *i.e.* physical remnants from the life of Christ or remains of a saint, such as a piece of bone, textile or paper. The Scripture refers to the healing power of objects that were touched by Christ or his Apostles. Thus, relics were greatly venerated and became the centre of pilgrimage throughout Europe. Many relics are kept in special containers, so called reliquaries, in the form of highly decorated caskets. More complex reliquaries have been designed, usually mimicking the relic it enshrined, such as an arm or a hand (Diedrichs, 2000).

In some cases relics have been hidden inside an art object without any external physical evidence of the relic's presence. This seems to have been the practice notably with sculpture, and in some rare instances also with altarpieces. A good example is the Norfolk triptych from the collection of the Museum Boymans-van Beuningen in Rotterdam (Fig. 1), which is considered one of the oldest paintings in The Netherlands. The main scene in the central panel represents the Deposition of Christ. The X-ray transmission radiography from this area shows that an inset was made into the panel, into which a thin plank of softwood was inlaid with its grain

direction perpendicular to the grain direction of the altarpiece (Van Grevenstein-Kruse, 1994). The reverse of the panel shows no sign of that inlay. The grain of the wood appears regular and no indication of a knot in the wood can be found. Art historians have therefore suspected the presence of some sort of flat relic. It should be noted that the Norfolk triptych is not an isolated case of a possible panel reliquary, as is exemplified by a panel with fragments of the veil of the Holy Virgin from the Basilica of Our Lady in Tongeren (Fremout *et al.*, 2006). Pending adequate visualization of a possible hidden object, the Norfolk triptych has not been studied further.

Regular X-ray transmission radiography has failed to properly image what is hidden behind the panel inlay. This is due to two basic limitations of radiography. First, the image provides no three-dimensional insight into the construction of the inlay. How deep is the inlay? How much space is left between the inset and the panel of the altarpiece itself? More important, however, is the limited sensitivity of X-ray absorption to low-Z materials. The paint layer on the front contains heavy metals like lead (Pb) and mercury (Hg) in pigments such as lead white and cinnabar. The wooden carrier has a thickness of about 4 cm. Any organic materials such as paper or textile sandwiched in between the paint and the wood are therefore virtually transparent at the relatively

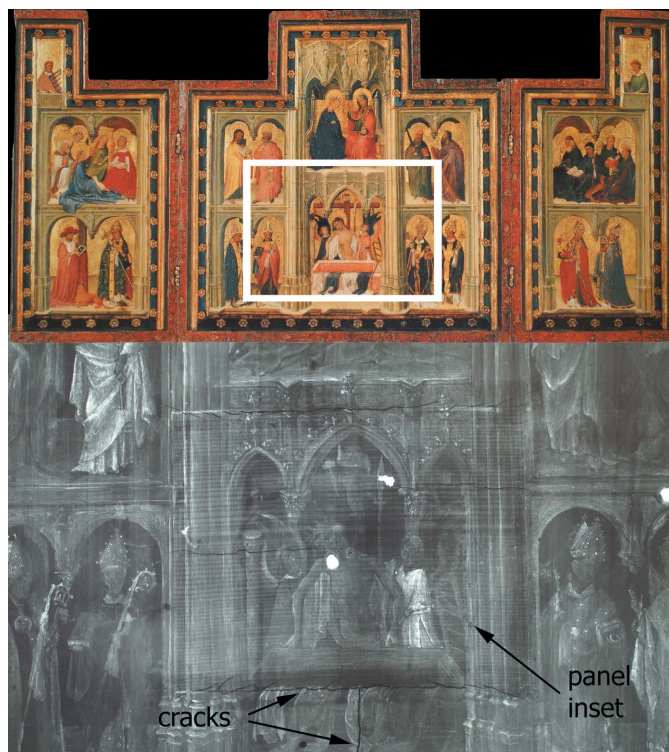


**Figure 1**  
Christ as the man of Sorrows, also known as the ‘Norfolk tryptych’ ca. 1415–1420, centre panel 33 cm × 32 cm, side panels 33 cm × 13 cm (Museum Boymans-van Beuningen, Rotterdam, The Netherlands). The white frame corresponds to the X-ray radiography of the central panel showing the wooden inlay and its perpendicular grain direction.

high energies needed to penetrate the entire object (>25 keV).

The present paper describes the first-time application of two synchrotron-based imaging techniques in the study of paintings: X-ray tomography and laminography, partly complemented with phase-contrast capabilities. These methods nicely complement other synchrotron imaging techniques that have been successfully applied to paintings in earlier studies (Krug *et al.*, 2006; Dik *et al.*, 2005).

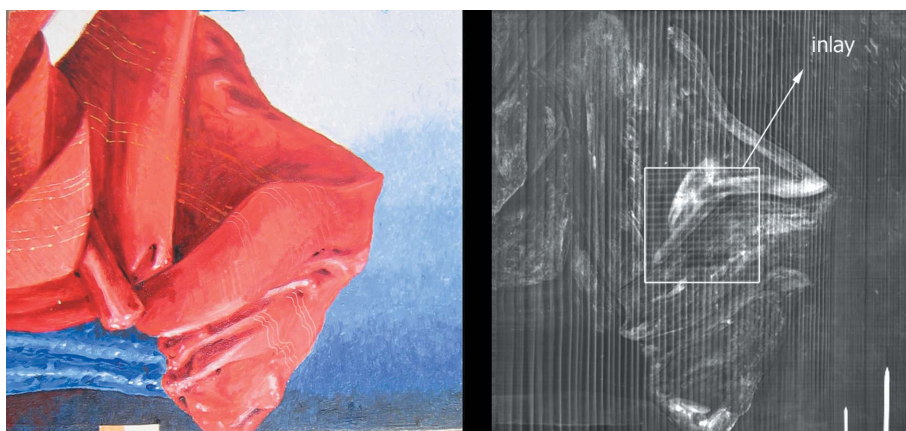


**Figure 2**  
Picture of the dummy painting and conventional X-ray radiograph showing inlay (white frame) with horizontal grain direction.

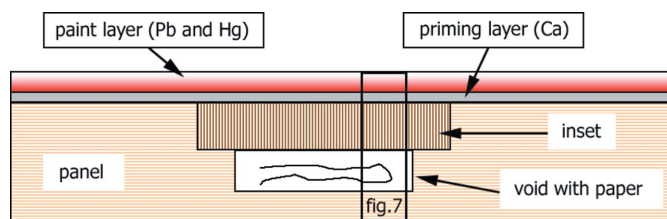


**Figure 3**  
Schematic cross section of the dummy panel showing the panel, inlay, grain directions and void, as well as the folded piece of paper. The frame indicates the field of view in Fig. 7.

## 2. Methodology

We prepared a test panel of size 15 cm × 15 cm × 2 cm of softwood, into which a small inset was cut, mimicking the suspected construction of the Norfolk panel. Behind the inset we placed a small folded piece of paper, with a short inscription in organic ink (‘Lieve God, mag ik een broodje kaas?’, *i.e.* ‘Dear God, could I please have a cheese sandwich?’). The panel was given an authentic chalk-based priming layer and several layers of various paints containing heavy metals like Hg and Pb. The panel’s visible light photograph and conventional X-ray radiography as well as the schematic stratigraphy are represented in Figs. 2 and 3, respectively. The test panel was examined at two beamlines, ID17 and ID19, at the European Synchrotron Radiation Facility (ESRF) in Grenoble, France.

### 2.1. Computed tomography

Tomographic imaging techniques such as X-ray computed tomography (CT) allow the non-destructive study of hidden structures inside an object. CT is an established technique at synchrotron imaging set-ups. CT yields best (*i.e.* mathematically correct) results if the object does not exceed the field of view of the two-dimensional detector system. This is accomplished by the scanning of the object from all directions around a single rotation axis. This corresponds to the complete sampling of the three-dimensional Fourier domain within certain resolution limits imposed by the detector system.

The CT imaging was carried out at ID17, the biomedical beamline. The source of radiation is a 6 GeV electron storage ring coupled to a 21-pole wiggler. In this experiment we used a 60 mm wiggler gap (0.6 T) which corresponds to a critical energy of 14.8 keV; this choice constitutes a good compromise between the available flux and the higher-energy harmonics content. A quasi-monochromatic (0.1% bandwidth) X-ray beam of 27.6 keV, corresponding to an energy just above the cadmium *K*-edge, was selected from the continuous X-ray spectrum using a double bent Laue silicon crystal mono-

chromator (Suortti *et al.*, 2000). At the sample position (about 145 m from the source) the vertical and horizontal widths of the beam were 0.6 mm and 150 mm, respectively. A detailed description of the synchrotron instrumentation can be found by Elleaume *et al.* (1999).

A high-precision computer-controlled stage with seven degrees of freedom (Spretec, Grenoble, France) was used for the positioning of the test panel and to scan it through the laminar beam during the image acquisition (Dabin *et al.*, 2001). Images were acquired by a high-purity germanium detector (EurisyS Measure, Lingolsheim, France) with horizontal pixel size of 350  $\mu\text{m}$  (Bravin *et al.*, 2003; Peterzol *et al.*, 2006). The detector operated in the charge-collecting mode, and acquisition was synchronized with the panel motion. The rotation speed in CT imaging was  $100^\circ \text{ s}^{-1}$  and images were recorded from 1024 angular projections acquired over  $360^\circ$ . Sequential 350  $\mu\text{m}$  slices were acquired to cover the full canvas. CT images were reconstructed using the filtered-back-projection algorithm with a Hamming filter.

### 2.2. Computed laminography

Computed laminography (CL), also known as digital tomosynthesis, was recently introduced at synchrotron imaging beamlines (Helfen *et al.*, 2005). CL is used to extend the applicability of tomographic synchrotron imaging to laterally large objects. Despite being intrinsically affected by imaging artifacts owing to incomplete sampling, the technique enables three-dimensional imaging of regions of interest in flat, laterally extended objects. Up to now this new technique has mainly been used for inspection of microsystem devices (Helfen *et al.*, 2006).

For the laminography measurements at ESRF's imaging beamline ID19, an X-ray energy of 26 keV was provided by an 11-pole wiggler at a gap of 40 mm (0.92 mm Al filter), corresponding to 23.7 keV critical energy, employing a double-crystal monochromator using Si 111 reflections. This yielded a beam size of 15.4 mm  $\times$  13.4 mm. A CCD-based detector system providing a pixel size of 7.5  $\mu\text{m}$  was chosen. In order to obtain sufficient image contrast, a propagation distance (see §2.3) of approximately 850 mm was used. A recently developed dedicated laminography instrument enables scanning of any region of interest on 150 mm  $\times$  150 mm-sized samples at tomographic angles ranging from  $45^\circ$  to  $70^\circ$  axis inclination of the rotation axis with respect to the transmitted X-ray beam. An inclination of  $57.1^\circ$  was chosen for the experiments presented here. A schematic drawing of the computed laminography set-up is shown in Fig. 4.

### 2.3. Phase-contrast imaging

As opposed to attenuation of radiation in conventional imaging, phase-contrast imaging shows refraction of the radiation caused by the spatial distribution of the refractive index in the object or non-uniform object thickness. In the case of propagation-based phase-contrast imaging, propagation of the X-ray wavefield leads to interference of wavefield components diffracted under different angles if the incident

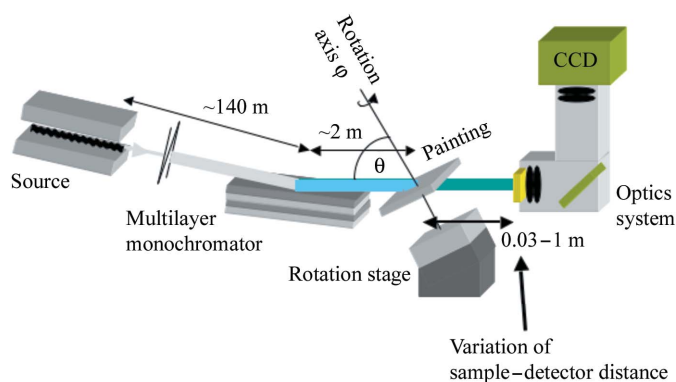


**Figure 4**  
Schematic drawing of the computed laminography set-up.

beam is partially coherent (Cloetens *et al.*, 1997). Using suitable propagation distances, internal interfaces between materials can be imaged owing to an increase of contrast between materials of different refractive index, an effective edge enhancement.

For the case of analyzer-based imaging (ABI), different refraction directions can be resolved by using a perfect crystal as an angular analyzer since refraction of an incident beam can be considered to occur at characteristic angles. By varying the alignment of the analyzer with regard to the incoming X-ray beam, the refracted X-rays can either be recorded on a detector or rejected, thus, either contributing or not contributing to the image contrast (Bravin, 2003).

For the measurements in this study, the ABI set-up available at ID17, and described in detail by Fiedler *et al.* (2004) and Keyriläinen *et al.* (2005), has been used. Briefly, the X-ray diffraction optics consisted of a symmetrically cut Si (111) Bragg monochromator and analyzer crystals in the non-dispersive setting. A thin fan-shaped (95 mm wide and 0.6 mm high) quasi-monochromatic X-ray beam of 38 keV was used in this experiment. The energy bandwidth ( $\Delta E/E$ ) of the beam was  $\sim 10^{-5}$ . The distance between the sample and the detector was about 2 m. Projection images were acquired by scanning the sample in front of the detector vertically through the monochromatic beam. The ABI images were taken at several different angular positions on the Si (111) analyzer rocking curve. A schematic drawing of the analyzer-based imaging set-up is shown in Fig. 5.

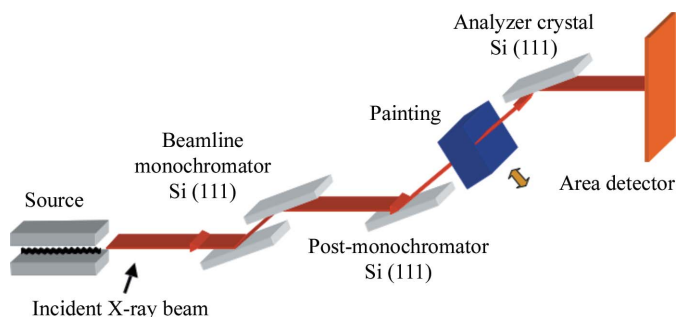


**Figure 5**  
Schematic drawing of the analyzer-based imaging set-up.

### 3. Results

#### 3.1. Computed tomography

A CT reconstruction of the test panel is presented in Fig. 6. The pixel size of the image is  $350\ \mu\text{m} \times 350\ \mu\text{m}$ , and image dimensions are  $35\ \text{mm} \times 170\ \text{mm}$ . White areas indicate high attenuation of the radiation.

#### 3.2. Computed laminography

A CL reconstruction of a region of interest (ROI) from the central part is presented in Fig. 7. The voxel axes of the reconstructed data set are  $7.5\ \mu\text{m}$ , and ROI dimensions are  $4.3\ \text{mm} \times 4.3\ \text{mm} \times 10\ \text{mm}$ . Bright areas indicate high attenuation of the radiation with a contribution due to edge enhancement by propagation-based phase contrast. Image contrast in the reconstructed data is strongly augmented to emphasize the interior of the panel, exhibiting the void containing the paper. Therefore, the paint layers at the top of the slice are saturated to a large extent. Despite the rather low signal-to-noise ratio in the reconstructed data, the three-dimensional structure of the chosen ROI can be rendered three-dimensionally.

#### 3.3. Analyzer-based imaging

Figs. 8 and 9, as well as Fig. 10, were produced using ABI. White and dark areas indicate higher and lower photon counts, respectively. Some of the vertical bands in the images are artifacts caused by variations in detector gain. The ABI analyzer strongly rejects scattered X-rays out of the horizontal plane of the analyzer. Scatter perpendicular to this plane is practically unaffected. Two sets of images were taken, one with the analyzer oriented perpendicular to the grain of our panel and one parallel to the wood grain. For the latter image set the test panel was turned  $90^\circ$  in the imaging set-up and flipped back to front.

**3.3.1. Panel grain oriented perpendicularly to the analyzer.** In the images presented in Fig. 8 the ABI analyzer is oriented horizontally. The scan direction is top-to-bottom.

**3.3.2. Panel grain oriented parallel to the analyzer.** In these images, presented in Fig. 9, the ABI panel has been rotated  $90^\circ$  during image acquisition, so that the grains are now parallel to the analyzer. For sake of clarity, images are shown in the same orientation as in Fig. 8, but in this case the line scan direction was left to right in the figure.

The images in Fig. 10 show details of letters from the inset area (lower right-hand corner of inset in Figs. 8 and 9). These images are presented with approximately the same contrast.

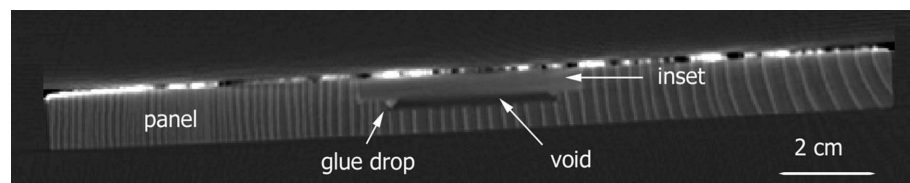


**Figure 6**  
Absorption CT image of the panel.

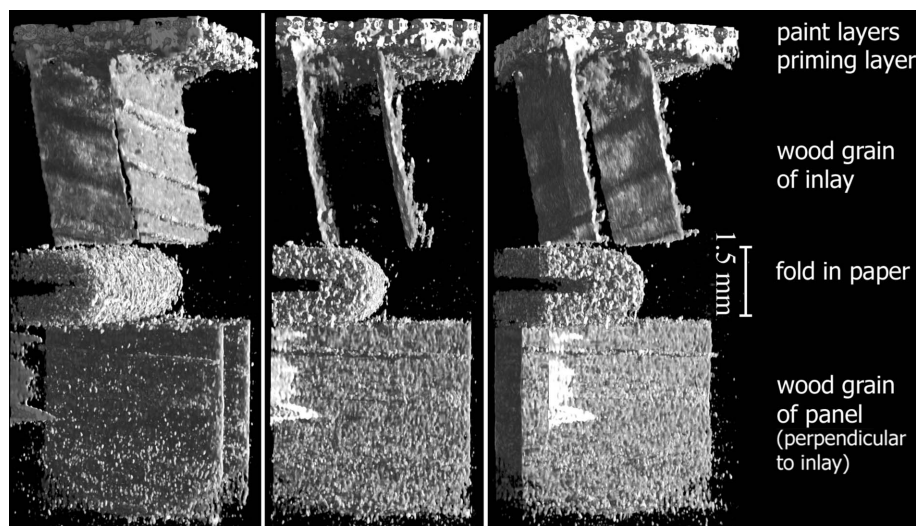


**Figure 7**  
Three-dimensional rendering of the panel under different viewing angles, obtained by synchrotron-radiation computed laminography. The paint layer at the top, the perpendicular grain directions in the inlay (below) and the panel (bottom), and the folded paper (centre) are clearly visible. The field of view is that indicated in Fig. 3. An animated  $360^\circ$  rotational view has been deposited and is available as supplementary data from the IUCr electronic archives (Reference: GF5005). Services for accessing these data are described at the back of the journal.

### 4. Discussion

#### 4.1. Computed tomography

The CT reconstruction nicely images the inner structure of the panel. This includes grain directions of the bulk panel, positioning of the panel inset and the void between the inset and the bulk panel. On both sides of the inset we noticed blobs of glue that were pressed into the void. Also note the variation in the year rings on the bulk panel. However, no traces of the hidden piece of paper could be visualized, let alone the writing on top.

#### 4.2. Computed laminography

The CL reconstruction of the test panel is able to visualize the hidden piece of paper. Imaging of a three-dimensional ROI enables a high spatial resolution to be attained in comparison with the CT measurement. Thus, the fibrous material of the paper becomes clearly visible as well as the grain structure of the wood. Also, the different layers of the paint can be separated which could enable investigations concerning its stratigraphy. The

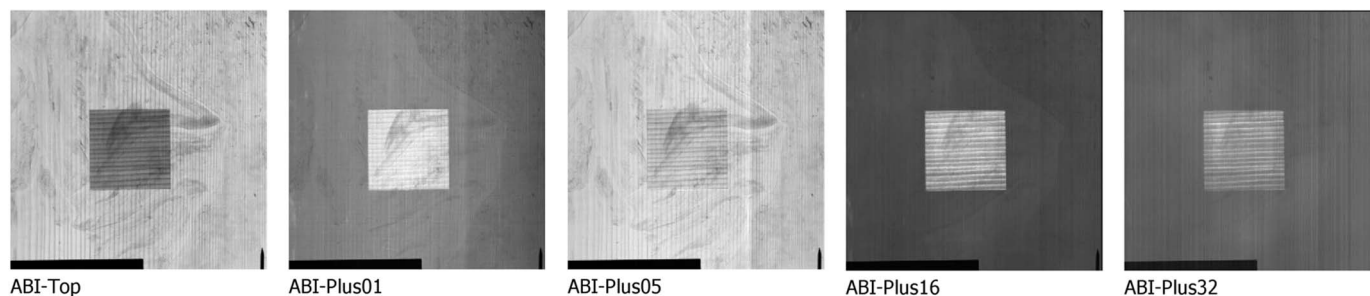


**Figure 8**  
ABI images with the panel grain oriented perpendicularly to the analyzer. Numbers refer to the angular shift of the analyzer (in microradians) with respect to the Bragg angle.

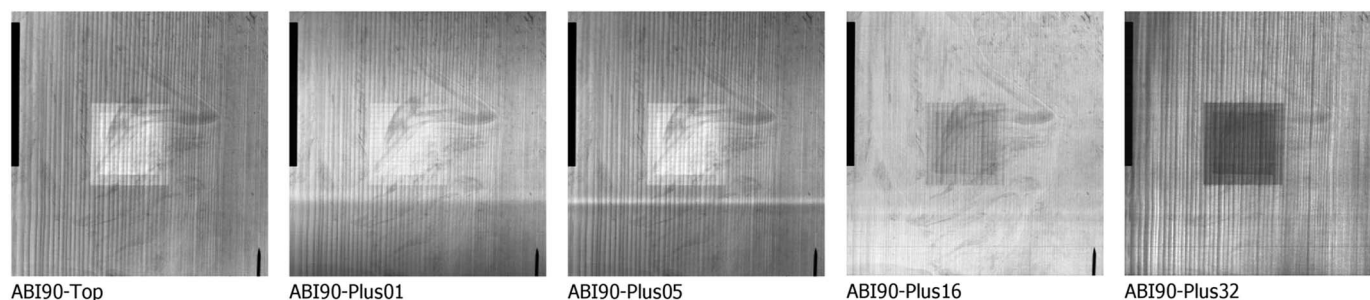


**Figure 9**  
ABI images with the panel grain oriented parallel to the analyzer. Numbers refer to the angular shift of the analyzer (in microradians) with respect to the Bragg angle.

Image	Panel grain to analyzer orientation	Refraction angle in microradians	Image comments
	Parallel	0 (ABI90-Top)	
	Parallel	+1 (ABI90-Plus01)	Optimum view on letters Ke(k) ?. Effects due to grain variations and background scatter is minimized.
	Parallel	+5 (ABI90-Plus05)	
	Perpendicular	+1 (ABI-Plus01)	

**Figure 10**  
Details of the upper right-hand corner of the inset showing letter contours on the paper, taken under different geometries of the ABI set-up.

letters written on the paper could not be found, however.

### 4.3. Analyzer-based imaging

It was observed that the hidden paper as well as the grain pattern of the wood could be imaged using ABI. However, this depended strongly on the rocking angle as well as the orientation of the grain direction *versus* analyzer plane. Images made with the ABI analyzer parallel to the wood grain gave the best images of the hidden paper, whereas the perpendicular orientation yielded poor signal contrast. In the parallel orientation images, most rocking-curve positions showed a dominant contribution of the wood grain. In the +16  $\mu\text{rad}$  image, however, the wood grain is almost absent, so that other features, notably paper and brushstrokes, are nicely visible.

These observations can be explained as follows. Wood consists primarily of one-dimensionally oriented columnar structures of cellulose that comprises approximately 50% of its mass (Miller, 1999). The cellulose molecules are arranged into strands called fibrils, which make up the cell walls of the wood fibers. Most of this

cellulose is crystalline. X-ray diffraction studies of wood have determined the molecular structure of cellulose and fibrils (Paakkari & Serimaa, 1984). Each cellulose crystal is about 2–4 nm in size and is arranged into fibrils that measure about 4 nm × 60 nm (Wood Ultrastructure Research Center at the Swedish University of Agricultural Sciences, <http://www-wurc.slu.se/>). These structures are arranged into fibers that are hollow tubes about 20–40 μm in diameter with 1–10 μm-thick walls, which are cemented together with lignin. These tubes serve to transport water and nutrients and provide the rigid structure to support the living tree. The tubes are created with thinner cell walls early in the growing season, the less-dense earlywood, and have thicker walls late in the growing season, the more-dense latewood. These density variations create the annual tree rings seen in a tree cross section.

ABI provides an image of X-rays that are refracted through very small angles of the order of a few microradians. These X-rays are scattered because of small periodic differences in the X-ray index of refraction in the medium. In the case of wood, the medium consists of ordered arrays of air and cellulose. These arrays have a short- to medium-range order that causes an anisotropy in the refracted X-rays dependent on the grain orientation.

A section of the bulk wood panel (not including the inset area) was analyzed using ABI in both grain-parallel and grain-perpendicular orientations. The same section of the bulk wood was examined at each of the rocking angles. By utilizing the image values in the top (zero refraction angle, *i.e.* Bragg angle) image which are primarily due only to density variations in the wood material, a map was created that classified each pixel as earlywood or latewood. The image pixels in the series of images were classified using this map and the average pixel values were plotted (Fig. 11)

Each orientation had a distinctly different pattern, yet both had a sharp notch at a slight angle, 1 μrad. This effect is especially pronounced when examined with the ABI analyzer oriented perpendicular to the wood grain. This notch provides a ‘window’ of low scatter from the bulk wood, most scatter occurring at other angles. If there are other scatter sources in the path different than the wood, these can ‘shine through’ and be seen against the background. This is shown clearly in the ABI90-Plus01 images of the letters on the paper in Fig. 10.

The response also varies with respect to latewood and earlywood areas. At certain angles the response is identical and the grain pattern disappears from the images. This explains the clear view on the paper and brushstrokes in the +16 μrad parallel-to-grain ABI image.

Paper is also composed of cellulose and wood fibers. These fibers, however, have been processed and ‘de-lignified’ and are arranged more randomly. Paper, therefore, does not have the same structure as wood and refracts more isotropically. The refraction characteristics of paper are significantly different than wood and show no notch. Writing on the paper would serve primarily to attenuate X-rays and refracted X-rays would show this attenuation as well.

The paper, and the writing on the paper, can therefore best be seen against the background of the wood panel when

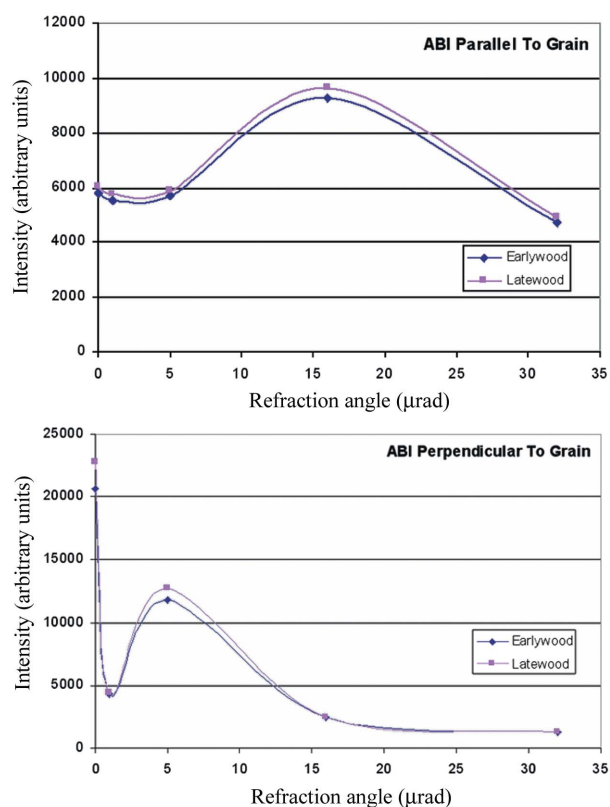


**Figure 11** Graphs showing intensity variations for latewood and earlywood of the test panel at different rocking-curve positions with parallel and perpendicular grain-to-analyzer orientation.

refracted X-rays image the wood panel at the angle of this characteristic notch. This is where the background, refracted radiation from the bulk wood, is at a minimum and the refracted radiation from the paper is still relatively high.

The images in Fig. 10 show a detail of the area of the wood test panel where the paper with letters is behind the inset. Four separate orientations and angles are shown. The best image with highest contrast for the written letters is with the bulk wood orientation perpendicular to the ABI analyzer at a rocking angle of 1 μrad, ABI90-01. Other orientations show poorer contrast for the letters.

### 5. Conclusion

Our study has shown that synchrotron-based tomographic and laminographic imaging complemented with phase-contrast capabilities are promising tools in the study of panel paintings. We constructed a dummy panel with an inscribed piece of paper hidden behind a wooden inset in the bulk panel, mimicking the suspected construction of the Norfolk tryptych.

A computer tomography scan with 0.35 mm resolution provided the three-dimensional structure of the entire panel, visualizing features such as wood grain, accumulations of glue and voids inside the panel. Computed laminography with micrometre spatial resolution allowed us to image local volumes, *i.e.* three-dimensional regions of interest, of the

panel. In combination with propagation-based phase-contrast imaging we succeeded in three-dimensionally imaging the piece of paper sandwiched among the wooden inset, the heavy metal paint layers and the bulk panel. This phase-contrast capability proved to be very effective in suppressing the otherwise dominant attenuation factor of surrounding high-Z materials, while strengthening the contrast of material interfaces in the panel.

In addition to the propagation-based set-up we also imaged our panel with analyzer-based phase-contrast imaging. With this phase-contrast method, which is particularly adapted to the detection of steady variations of the projected refractive index distribution, we not only imaged the hidden paper but were also able to bring out contours of the ink writing on the paper. The contrast in these images strongly depended on the refraction angle, the ABI orientation with respect to the wood grain and, to a lesser extent, the density of the grain being imaged. The future availability of a laminography set-up using an analyzer-based phase contrast could significantly improve the detectability of such written texts.

We would like to thank Dr J. Giltaj from the Museum Boymans-van Beuningen for helpful discussions and allowing us to use existing X-ray images.

## References

- Bravin, A. (2003). *J. Phys. D*, **36**, 24–29.
- Bravin, A., Fiedler, S., Coan, P., Labiche, J. C., Ponchut, C., Peterzol, A. & Thomlinson, W. (2003). *Nucl. Instrum. Methods A*, **510**, 35–40.
- Cloetens, P., Pateyron-Salomé, M., Buffière, J. Y., Peix, G., Baruchel, J., Peyrin, F. & Schlenker, M. (1997). *J. Appl. Phys.* **81**, 58–78.
- Dabin, Y. *et al.* (2001). *Nucl. Instrum. Methods A*, **467**, 1342–1345.
- Diedrichs, C. (2000). *Vom Gauben zum Sehen: die Sichtbarkeit der Reliquie im Reliquar: ein Beitrag zur Geschichte des Sehens*. Berlin: Weissensee.
- Dik, J., Krug, K., Den Leeuw, M. & Bravin, A. (2005). *Z. Kunstst. Kons.* **28**, 315–322.
- Elleaume, H. *et al.* (1999). *Nucl. Instrum. Methods A*, **428**, 513–527.
- Fiedler, S., Bravin, A., Keyriläinen, J., Fernández, M., Suortti, P., Thomlinson, W., Tenhunen, M., Virkkunen, P. & Karjalainen-Lindsberg, M. L. (2004). *Phys. Med. Biol.* **49**, 175–188.
- Fremout, W., Saverwyns, S., Peters, F. & Deneffe, D. (2006). *J. Raman Spectrosc.* **37**, 1035–1045.
- Helfen, L., Baumbach, T., Mikulik, P., Kiel, D., Pernot, P., Cloetens, P. & Baruchel, J. (2005). *Appl. Phys. Lett.* **86**, 071915.
- Helfen, L., Myagotin, A., Pernot, P., DiMichiel, M., Mikulik, P., Berthold, A. & Baumbach, T. (2006). *Nucl. Instrum. Methods A*, **563**, 163–166.
- Keyriläinen, J., Fernández, M., Fiedler, S., Bravin, A., Karjalainen-Lindsberg, M. L., Virkkunen, P., Elo, E. M., Tenhunen, M., Suortti, P. & Thomlinson, W. (2005). *Eur. J. Radiol.* **53**, 226–237.
- Krug, K., Dik, J., Den Leeuw, M., Whitson, A., Tortora, J., Coan, P., Nemoz, C. & Bravin, A. (2006). *Appl. Phys. A*, **83**, 247–251.
- Miller, R. B. (1999). *Wood Handbook*, revised ed. Washington: US Department of Agriculture.
- Paakkari, T. & Serimaa, R. (1984). *Wood Sci. Technol.* **18**, 79–85.
- Peterzol, A., Bravin, A., Coan, P. & Elleaume, H. (2006). *Radiat. Prot. Dosim.* **117**, 44–49.
- Van Grevenstein-Kruse, A. (1994). *Report on the Treatment of the Norfolk Tryptich, Van Eyck to Breughel, 1400 to 1550: Dutch and Flemish Painting in the Collection of the Museum Boymans-van Beuningen*, edited by J. Giltay, pp. 10–17. Rotterdam: Museum Boymans-van Beuningen.
- Suortti, P., Fiedler, S., Bravin, A., Brochard, T., Mattenet, M., Renier, M., Spanne, P., Thomlinson, W., Charvet, A. M., Elleaume, H., Schulze-Briese, C. & Thompson, A. C. (2000). *J. Synchrotron Rad.* **7**, 340–347.